Extreme-ultraviolet lensless Fourier-transform holography

Sang Hun Lee, Patrick Naulleau, Kenneth A. Goldberg, Chang Hyun Cho, SeongTae Jeong, and Jeffrey Bokor

We demonstrate 100-nm-resolution holographic aerial image monitoring based on lensless Fourier-transform holography at extreme-UV (EUV) wavelengths, using synchrotron-based illumination. This method can be used to monitor the coherent imaging performance of EUV lithographic optical systems. The system has been implemented in the EUV phase-shifting point-diffraction interferometer recently developed at Lawrence Berkeley National Laboratory. Here we introduce the idea of the holographic aerial image-recording technique and present imaging performance characterization results for a 10× Schwarzschild objective, a prototype EUV lithographic optic. The results are compared with simulations, and good agreement is obtained. Various object patterns, including phase-shift-enhanced patterns, have been studied. Finally, the application of the holographic aerial image-recording technique to EUV multilayer mask-blank defect characterization is discussed. © 2001 Optical Society of America

OCSI codes: 070.2590, 070.2580, 050.1950, 050.1960, 050.5080, 220.3740.

1. Introduction

The fabrication of electronic devices with ever-smaller feature sizes is an ongoing challenge for the integrated-circuit manufacturing community. Recently, the industrial standard critical dimension for integrated-circuit devices has dropped from 0.25 to 0.18 μm. Further progressions to critical dimensions of 0.1 μm are anticipated by means of extending conventional optical lithography methods to shorter wavelengths. For critical dimensions beyond 0.1 μm, however, new lithographic techniques may be needed. One promising candidate is extreme-UV (EUV) lithography. This method continues on the path of projection optical systems but with a radical reduction in wavelength (10–15 nm) and conversion to lower-numerical-aperture (N.A.) all-reflective systems. EUV systems require unprecedented fabrication tolerances and hence unprecedented metrology accuracy.[1] Here we describe an at-wavelength holographic image-recording technique developed to monitor the coherent imaging performance of high-quality EUV lithographic optical systems.

In holography, when a suitably coherent reference wave front interferes with an arbitrary wave front emanating from some object distribution, electric field information, including amplitude and phase, can be recorded. This holographic information can be used to reconstruct the original object distribution. Holography may also be applied to recording a virtual object distribution such as an aerial image produced by an optical system, thus characterizing the optic's coherent imaging performance. An advantage of using holography to monitor the coherent imaging performance is that electric field information including phase and amplitude, rather than simply intensity, can be obtained.[2] The holographic aerial image-recording technique is also attractive because of its compactness and its ability to monitor the image without printing in photoresist. Although this holographic method imposes a coherent imaging condition on the system under test, whereas lithographic printing typically employs partially coherent light, the partially coherent imaging performance can be predicted from the coherent image.

In this study, lensless Fourier-transform holography[3] is employed to record the aerial images, produced by prototype EUV lithographic optics. This system is readily implemented by modification of the EUV phase-shifting point-diffraction interferometer

S. H. Lee (shlee@lbl.gov), C. H. Cho, and F. Bokor are with the Department of Electrical Engineering and Computer Sciences, University of California, Berkeley, Berkeley, California 94720. S. H. Lee, P. Naulleau, K. A. Goldberg, C. H. Cho, S. T. Jeong, and J. Bokor are with the Center for X-Ray Optics, Lawrence Berkeley National Laboratory, Berkeley, California 94720.

Received 9 May 2000; revised manuscript received 13 February 2001.

0003-6935/01/162655-07$15.00/0

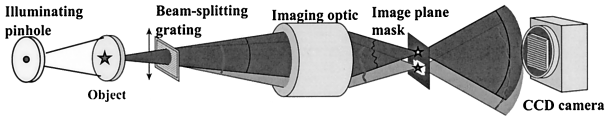

Fig. 1. Lensless Fourier-transform holography technique for recording lithographic aerial images. The system is obtained by slight modification of the PS/PDI system. The object is illuminated with coherent light.

(PS/PDI), which is described in detail elsewhere.[4–6] Lensless Fourier-transform holography is described as follows. A coherent wave scattered by the object propagates to the far-field recording plane. The free-space propagation has the effect of Fourier transforming the object wave. A coherent, well-defined reference wave is introduced on a spatial carrier to interfere with the object wave in the recording plane. Thus an off-axis hologram of the object distribution Fourier transform is recorded.

The lensless Fourier-transform holography system used in this study is shown in Fig. 1. The configuration is similar to that of the PS/PDI.[4–6] A spatial-filtering pinhole is used to illuminate the object with a coherent spherical wave front. The pinhole size is chosen to produce relatively uniform intensity illumination. A transmission grating is inserted between the object and the optical system under test to act as a beam splitter, producing multiple, laterally displaced, images of the object in the image plane. A mask containing a square window and spatial-filtering pinhole is placed in the image plane to select two of the orders diffracted by the grating. The first-order image passes through the window and will eventually serve as the object beam, whereas the zero-order image is made to fall on the pinhole filter that provides the spherical reference wave.

The two beams propagate to the CCD camera where they overlap, producing a hologram. The hologram captures a record of the aerial image produced by the optic under test as seen through the image-plane window; thus the lateral extent of the recorded image is limited by the size of this window.

2. Experimental Setup

The present setup for EUV holographic aerial image recording is depicted in Fig. 2. EUV radiation is provided by an undulator beam line (beam line 12.0.1 at the Advanced Light Source, Lawrence Berkeley National Laboratory). The beam line, containing a grating monochromator followed by a Kirkpatrick–Baez mirror pair, delivers radiation from the undulator to the holographic recording setup. The undulator beam line provides continuously tunable illumination from 5- to 25-nm wavelength with spectral resolving power as high as $\lambda/\Delta\lambda \sim 1000$. A flat multilayer-coated turning mirror is mounted at an angle of incidence near 45° to direct the beam vertically.

Near the focal plane of the Kirkpatrick–Baez pair, an illumination pinhole is used as a spatial filter to provide uniform and coherent illumination of the object. The pinhole is a commercially available 1.5-μm laser-drilled pinhole.

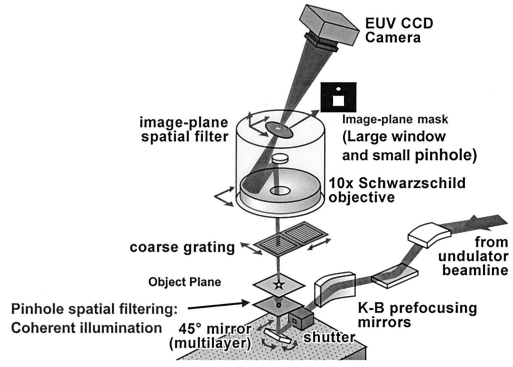

Fig. 2. Experimental configuration of the lensless Fourier-transform holography system. The coherent illumination at 13.4-nm wavelength is rendered by pinhole diffraction of the undulator beam.

The object-plane mask is placed ~15 mm above the illumination pinhole and can be readily replaced, allowing various structures to be studied. The binary masks used in this study were fabricated with electron-beam lithography. Nickel (Ni) is used as the absorber material patterned on top of a 100-nm-thick Si_3N_4 membrane. The phase-shift-enhanced masks used in this study were fabricated with optical lithography methods, and molybdenum (Mo) was used as the attenuating phase-shift material.

As described above, a grating beam splitter is placed between the object-plane mask and the entrance aperture of the imaging optic. This grating is typically 18-μm pitch with 20% duty cycle. The low duty cycle (mostly opened) is used to help balance the intensity of the two waves at the CCD plane.

The imaging optic we used in the experiment is a Schwarzschild objective with 10× demagnification, two spherical Mo/Si multilayer-coated mirrors, numerical aperture (N.A.) of 0.088, and 400-μm-diameter image-side field of view. The wave-front quality of the 10× optic has been measured with the PS/PDI to be $\lambda/13$ rms over 0.088 N.A. at a wavelength of 13.4 nm.[5,6] This particular optic suffers from ~40% flare, owing to the roughness of the mirror substrates.[1,7,8]

Owing to diffraction from the grating, multiple images of the object are formed at the image plane. The test beam window is a 3 μm × 3 μm square open area, and the reference pinhole, typically 50–150 nm in diameter, is placed 4.5 μm from the center of the window. The center-to-center separation is 1.5 times the window width in order to prevent any overlap between the holographic image and the zero-order image. The image-plane mask is fabricated with electron-beam lithography and reactive ion etching. The mask pattern is completely etched through a 1000-Å Si_3N_4 membrane, and then 1000 Å of Ni is evaporated on each side to provide the required EUV attenuation.

A CCD detector is placed in the far field, where the

two beams interfere, to generate the lensless Fourier-transform hologram. The detector is a backilluminated, backthinned, EUV CCD detector with 1024 × 1024 pixels over a 1-in.^{2} (~6.45-cm^2) area.

3. Data Analysis: Holographic Image Reconstruction

Recording and reconstruction of the Fourier-transform hologram is described as follows. The electric field of the aerial image centered in the test window is written as $u(\xi, \eta)$. Propagating this field to the CCD plane located in the far field yields $U(x, y)$. Similarly $T(x, y)$ is the far-field propagation of $t(\xi, \eta)$, which is simply a point source representing the reference pinhole. Because far-field Fraunhofer diffraction is related to the Fourier transform,[3] $U(x, y)$ and $T(x, y)$ are Fourier transforms of $u(\xi, \eta)$ and $t(\xi, \eta)$, respectively. Therefore the intensity pattern recorded at the CCD can be written as

$$I_{\mathrm{CCD}} = |U(x, y) + T(x, y)|^2 = U \times U^* + T \times T^* + U \times T^* + T \times U^*. \quad (1)$$

The reference field is generated by pinhole diffraction; thus $T(x, y)$ is approximated to be the Fourier transform of a delta function. Because the reference pinhole is displaced by s from the center of the image field in the image plane, $T(x, y)$ can be written as

$$T(x, y) = \mathrm{FT}\{\delta(\xi - s, \eta)\} = T_0 \exp[j2\pi(s/\lambda z)x]. \quad (2)$$

The goal of holographic reconstruction is to retrieve $u(\xi, \eta)$ from Eq. (1), which can readily be achieved by way of a simple Fourier transform, yielding

$$\mathrm{FT}\{I_{\mathrm{CCD}}\} = u \otimes u^* + t \otimes t^* + u \otimes t^* + t \otimes u^*, \quad (3)$$

where $u = \mathrm{FT}\{U(x, y)\}$, $t = \mathrm{FT}\{T(x, y)\}$, and 196 indicates convolution. Constants and coordinate scaling factor have been neglected. The first and the second terms in Eq. (3) are the autocorrelation functions of the image and the reference fields at the image plane, and the third and the fourth terms are the image field and its complex conjugate convolved with the reference field at the image plane. The autocorrelation functions correspond to unwanted dc terms. Since the reference field at the image plane is a displaced delta function, the third and the fourth terms yield the image field information, $u(\xi, \eta)$ and $u^*(\xi, \eta)$, displaced by s from the dc term.

Adequate separation between the pinhole and the window center is required in order to prevent the reconstructed image-field information, $u(\xi, \eta)$, from overlapping with the dc terms. The maximum size of the image-field distribution at the image plane is determined by the size of the test window. In Eq. (3) the first term, which is an autocorrelation function of the image field, has a maximum width of twice the test window size, and the third term has a maximum width of the test window size. To prevent the overlap between the first term and the third term, the displacement has to be larger than 1.5 times the maximum image field size, which in this case is the size of the test window.

The resolution of the holographic aerial image-recording technique depends on the reference pinhole diffraction; thus the pinhole size ultimately determines the smallest features that can be holographically reconstructed. In our experiment, pinhole sizes of ~100 nm in diameter were used. The diffraction angle determined by these pinholes corresponds to ~0.09 N.A., guiding a holographic resolution limit of ~100 nm.

4. Experimental Results

The system described here has been used to characterize the imaging performance of a recently fabricated 10×-reduction EUV Schwarzschild objective. The first object considered was a simple 15-μm-diameter circular aperture producing a 1.5-μm-diameter image. The recorded hologram and its Fourier transform are shown in Figs. 3(a) and 3(b). As described above, the off-axis terms in the Fourier

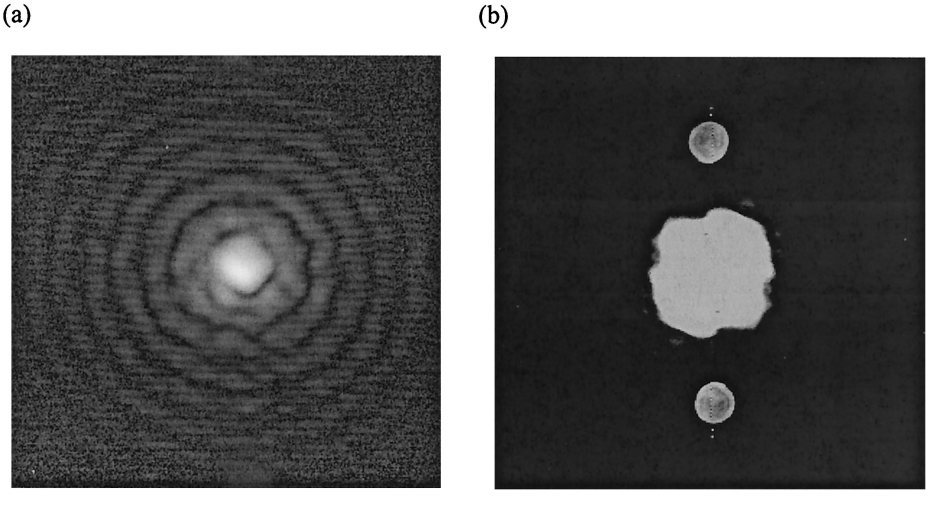

Fig. 3. Experimental results for a 1.5-μm image-side diameter circular aperture; (a) shows the recorded hologram and (b) its Fourier transform.

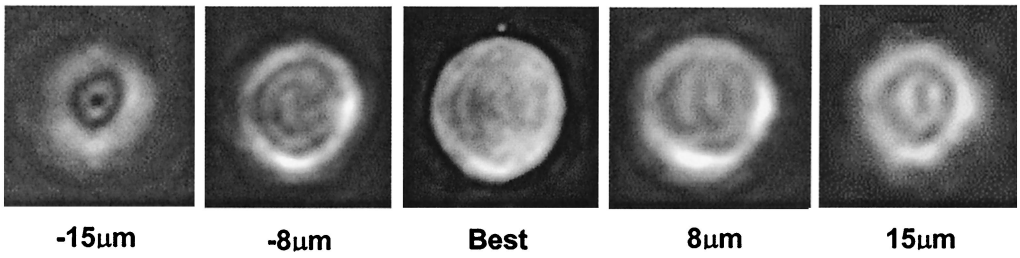

Fig. 4. Through focus images of a circular aperture. At the best focus the sharp-edged circular aperture image is clearly evident along with Fresnel ringing. The almost symmetric image quality through focus indicates the astigmatism to be well controlled in the optic under test.

transform represents the image-plane distribution and its complex conjugate, respectively.

By changing the longitudinal position of the image-plane mask, holograms of the images at various planes can be recorded. This provides for a convenient method of performing through-focus studies. Figure 4 shows the through-focus images of the 1.5-μm circular aperture reconstructed from the different holograms. At +15-μm defocus, Fresnel ringing is evident. As the longitudinal recording plane moves closer to the best focus, the edges are observed to sharpen, and the dark spot at the center begins to disappear. For the best focus image, the rings observed around the sharp edge are characteristic of the coherent imaging process employed here. As we pass through the best focus and go to the −15-μm defocus, similar images are observed, indicating a low level of astigmatism in this optic. The depth of focus of the optic was found to be ~1.1 μm, in good agreement with the theoretical value.

The next object considered was a star pattern with a continuous size variation from 0.3 to 3 μm. This object was used to demonstrate the resolution of the holographic aerial image-recording technique. Figure 5(a) shows the SEM picture of the star pattern object. A 1 μm × 1 μm square is located at the center of the pattern. The holographically reconstructed image of the star pattern is shown in Fig. 5(b). In Fig. 5(b) the largest feature size is 300 nm, and the isolated center spot corresponding to 100 nm is clearly reconstructed, indicating that the holographic aerial image-recording technique can resolve a feature size of at least 100 nm.

We note that the reconstructed image shown in Fig. 5(b) is partially obstructed by the image-plane window. The contour of the image plane window is represented by the dotted line in Fig. 5(b).

Figure 6 shows holographically reconstructed images of various objects. For the character-based images [Figs. 6(a)–(d)] the larger letters are composed of 200-nm-wide lines and the small letters of 100-nm-wide lines. Figures 6(e), 6(f), and 6(g) show 200-nm equal lines and spaces, 150-nm equal lines and spaces, and 100-nm 1:3 lines and spaces elbow patterns, respectively.

The speckle seen in Fig. 6 arises primarily due to flare in the optic under test.[2] The optic used here has previously been determined to experience approximately 40% flare.[7,8] Flare is caused by mid-spatial-frequency roughness on the mirrors and in

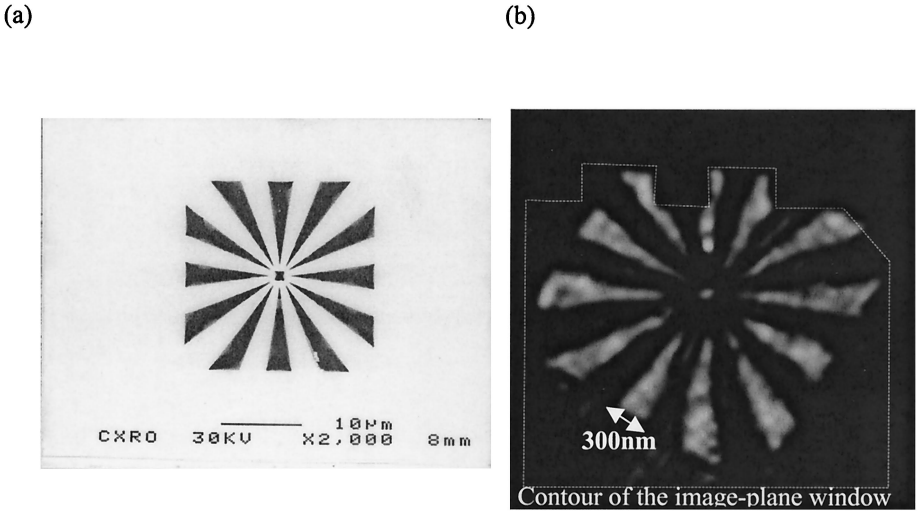

Fig. 5. (a) SEM picture of a star-pattern object. The size variation from 0.3–3 μm allows us to investigate the resolution of the holography. (b) The reconstructed image of the star pattern with the holography technique. The spot located at the center of the pattern is 100 nm in diameter. The partial obstruction due to the image-plane window is indicated by the dotted line.

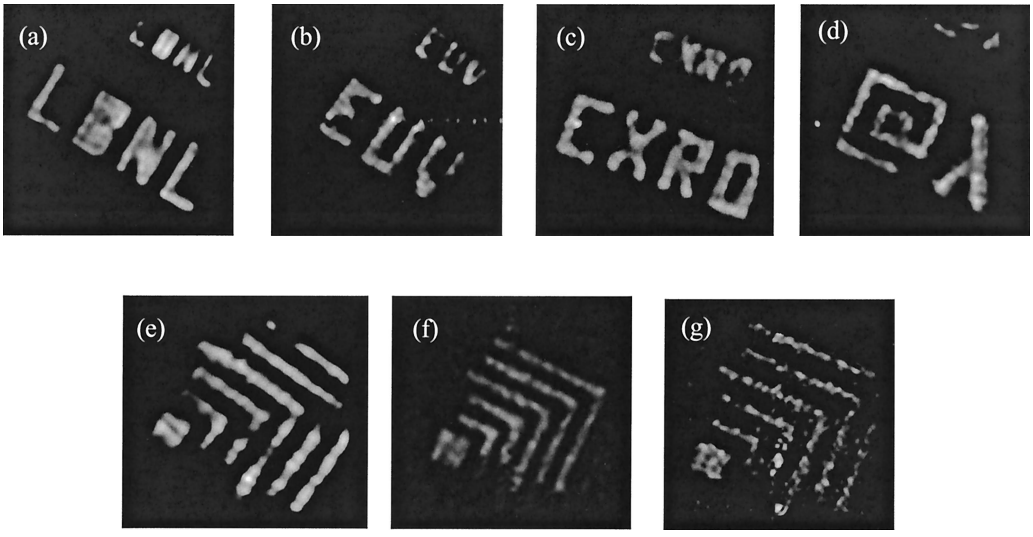

Fig. 6. Holographically reconstructed images of various objects. For the character-based images [(a)–(d)] the larger letters are composed of 200-nm-wide lines and the small letters of 100-nm-wide lines. (e), (f), and (g) show 200-nm equal lines and spaces, 150-nm equal lines and spaces, and 100-nm 1:3 lines and spaces elbow patterns, respectively.

conventional incoherent imaging systems leads to image-contrast reduction. In coherent systems such as that considered here, however, scatter leads to speckle with the size set by the diffraction-limited resolution of the optic under test. Furthermore, with the holographic method used here, if the resolution of the holographic recording is lower than the diffraction-limited test optic resolution, the speckle size will be set by the resolution of the holography.

5. Simulation of Coherent Imaging Performance of the 10× Schwarzschild Optic

The results obtained with the holographic aerial image-recording system have been verified by way of computer simulation with the Huygens–Fresnel principle.[3] The simulation calculates the coherent aerial image based on the known pupil function of the optic while ignoring the effect of flare. The pupil function is well known from previous PS/PDI characterizations.[5]

Referring to the geometry in Fig. 7, assume that an object is placed a distance z_1 in front of an imaging system and is illuminated by a monochromatic spherical wave. $U_{o(\xi,\eta)}$ represents the complex field immediately behind the object. The image plane of interest is taken to be a distance z_2 after the exit pupil, and the field in this plane is represented as

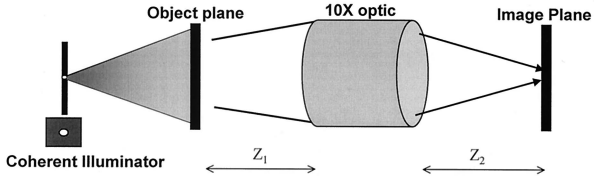

Fig. 7. Schematic depicting the simulation parameters. The simulation incorporates both the spherical object illumination and the aberration in the optic while ignoring the effect of flare. The optic aberration had been precisely determined with the PS/PDI.

$U_{i(u,v)}$. Because this system can readily be shown to be linear in electric field, $U_{i(u,v)}$ can be expressed by the following superposition integral:

$$U_i(u,v) = \iint_{\infty} [h(u,v;\xi,\eta) \times U_o(\xi,\eta)]\,\mathrm{d}\xi\mathrm{d}\eta, \quad (4)$$

where $h(u, v; \xi, \eta)$ is the impulse response of the system. Thus the properties of the coherent imaging system are completely described if the impulse response h can be specified. Equation (4) states that the image-field distribution is a two-dimensional convolution between the impulse response function and the properly scaled object field. The impulse response is readily determined from the known pupil function. In practice the calculation is simplified by use of the spatial-frequency representation of Eq. (4).

Figure 8 shows the simulation results for the various objects used experimentally. The simulation and experimental results are in good qualitative agreement. This agreement confirms that the holographic aerial image-recording technique can be used to monitor the coherent imaging performance of lithographic optical systems. The discrepancies between the two results (line edge roughness and speckle-induced background noise observed in the experimental data but not the simulation) are most likely due to neglecting flare in the simulation.

6. Attenuated Phase-Shifting Object

The most significant advantage of the holographic aerial image-monitoring technique is the ability to measure phase information as well as amplitude. This capability has been studied by way of phase-shift-enhanced Mo masks. At a wavelength of 13.4 nm, Mo can provide a phase shift of π with as much as ~60% intensity transmission.[9] These phase-

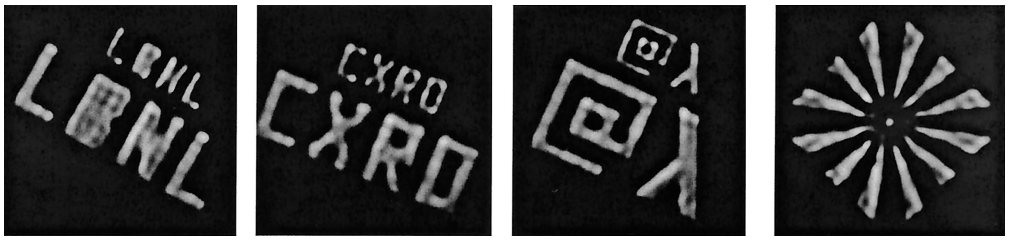

Fig. 8. Simulation results for various objects matching those used experimentally. Qualitative agreement with the experimental results is observed.

shifting masks were fabricated by patterning of Mo onto a Si_3N_4 membrane.

Low-stress, off-stoichiometric [silicon- (Si-) rich] low-pressure chemical vapor deposition (LPCVD) Si_3N_4 was deposited on both sides of a Si wafer. Mo was then deposited on the membrane by magnetron sputtering. To reduce the stress in the Mo film, the sputtering conditions were optimized. After deposition of the Mo, photolithography and etch processes were used to delineate the mask patterns. To protect the Mo patterns during the backside Si wafer etch, plasma-enhanced chemical vapor deposition (PECVD) oxide was deposited on top of the patterns. The Si wafer was etched in potassium hydroxide solution from the backside of the wafer, which stopped on the Si_3N_4 on the front side. The final structure for our EUV attenuated phase-shifting mask is an 860-Å-thick (π-phase-shift) patterned Mo layer on a 1000-Å-thick Si_3N_4 membrane. The visible microscope view of the phase-shifting mask of 5-μm equal lines and spaces is shown in Fig. 9, and its cross-section configuration is also depicted. The dark lines indicate Si_3N_4 regions, and bright lines indicate Mo regions.

Cross-section plots of the electric field, phase, and intensity of the holographically reconstructed image of the phase object are shown in Figs. 10(b), 10(c), and 10(d), respectively. The object mask cross section is shown in Fig. 10(a) for comparison purposes. Figure 10(b) shows that the electric field crosses zero at the edges of Mo patterns and that negative electric field is observed in the Mo regions. When the electric field is negative, the corresponding phase is close to π, indicating that proper Mo thickness has been achieved. Measured phase difference between the normal (Si_3N_4 region) and the phase-shifting (Si_3N_4 and Mo regions) regions ranged from 160° to 180° as shown in Fig. 10(c). Small discrepancies from π phase shift may due to phase ringing caused by the limited resolution and imperfections of the Mo layer thickness. This also reveals that, by measurement of the phase, the Mo thickness can be characterized. The intensity is the modulus squared of the field, and zero intensity points are observed between the normal and the phase-shift regions, owing to the electric field amplitude crossing zero at the phase step. Thus frequency doubling is evidenced when the in-

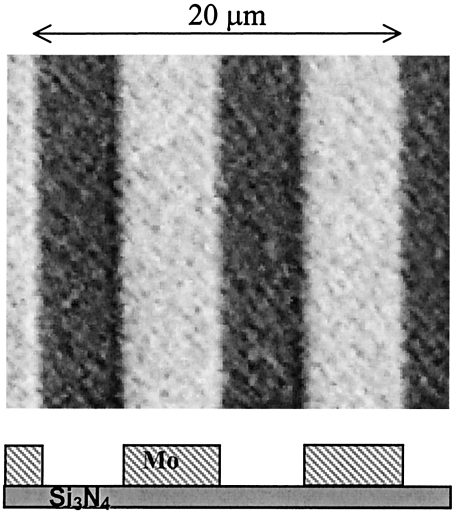

Fig. 9. Optical microscope image of the attenuated phase-shifting mask. The bright regions indicate the Mo layers. Pi phase-shifting is anticipated at the Mo regions.

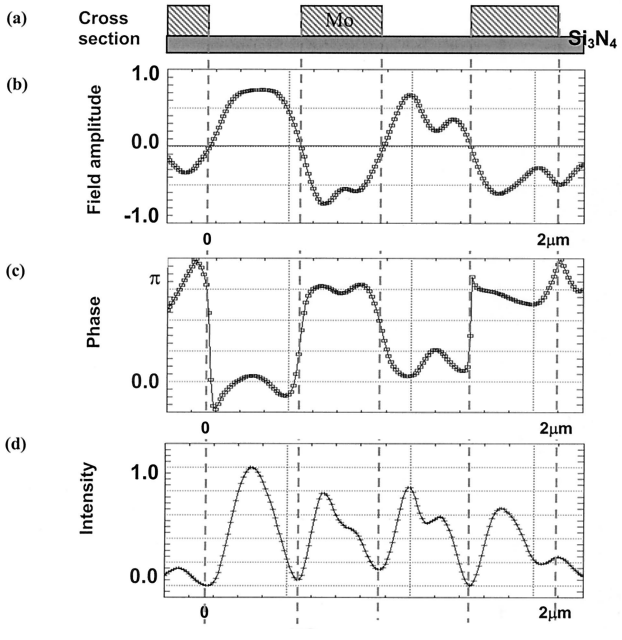

Fig. 10. Experimental results obtained with the phase-shift mask. (a) Cross-section view of the actual mask; (b) cross-section plot of the electric field, which is seen to go negative; (c) corresponding phase. π phase shifts are observed for Mo regions. (d) Intensity pattern obtained by the modulus squared of the plot (b), revealing frequency-doubling effect.

tensity image and the original object are compared. This attenuated phase-shifting mask is similar to chromeless phase-shift masks used in conventional lithography to enhance optical resolution.[10]

7. Applications of the Holographic Aerial Image-Recording Technique

The holographic aerial image-recording technique is a powerful tool that can characterize both phase and amplitude information of coherent images. With simple modifications this tool can be further applied to the microscopic characterization of isolated defects on EUV multilayer mask blanks. The quantitative understanding of mask-blank defects is a critical issue for EUV lithography.[11] Opaque and phase defects in and/or on the multilayer mask blank have to be identified in order to improve the mask fabrication processes. In principle, by use of the holographic method, full characterizations of opaque and phase defects are possible.[12] The holographic method is of particular interest because few other methods exist that can quantify both the phase and the amplitude of submicrometer-sized defects on EUV mask blanks.

8. Conclusion

Holographic aerial image recording has been introduced for the first time, to our knowledge, at the 13.4-nm wavelength. This holographic technique can be used to monitor coherent imaging performance of EUV lithographic optical systems. Images of various binary objects formed by a 10×-reduction Schwarzschild EUV optical system have been recorded and analyzed. The coherent imaging performance of the 10× optic has been simulated and compared with experimental results, and good qualitative agreement has been obtained. Also, by use of phase-shifting objects, the phase measuring capabilities of this system have been demonstrated. Future research should include applying this system to the characterization of isolated defects on EUV multilayer mask blanks.

References

1. D. Williamson, "The elusive diffraction limit," in *Extreme Ultraviolet Lithography*, D. Attwood and F. Zernike, eds., Vol. 23 of OSA Proceedings Series (Optical Society of America, Washington, D.C., 1994), pp. 68–76 (1995).
2. S. Lee, P. Naulleau, K. A. Goldberg, and J. Bokor, "EUV holographic aerial image recording," in *SPIE Microlithography Conference in Emerging Lithographic Technologies III*, E. A. Dobisz, ed., Proc. SPIE **3997,** 823–828 (2000).
3. J. Goodman, *Introduction to Fourier Optics*, 2nd ed. (McGraw-Hill, New York, 1996).
4. H. Medecki, E. Tejnil, K. A. Goldberg, and J. Bokor, "A phase-shifting point diffraction interferometer," Opt. Lett. **21,** 1526–1528 (1996).
5. K. A. Goldberg, P. Naulleau, and J. Bokor, "EUV interferometric measurements of diffraction-limited optics," J. Vac. Sci. Technol. B **17,** 2982–2986 (1999).
6. P. Naulleau, K. A. Goldberg, S. H. Lee, C. Chang, P. Batson, D. Attwood, and J. Bokor, "Recent advances in EUV phase-shifting point diffraction interferometry," in *EUV, X-Ray, and Neutron Optics and Sources*, C. A. MacDonald, K. A. Goldberg, J. R. Maldonado, H. H. Chen-Mayer, and S. P. Vernon, eds., Proc. SPIE **3767,** 154–163 (1999).
7. P. Naulleau, K. A. Goldberg, E. M. Gullikson, and J. Bokor, "Interferometric at-wavelength flare characterization of EUV optical systems," J. Vac. Sci. Technol. B **17,** 2987–2991 (1999).
8. E. M. Gullikson, S. L. Baker, J. E. Bjorkholm, J. Bokor, K. A. Goldberg, J. E. M. Goldsmith, C. Montcalm, P. Naulleau, E. A. Spiller, D. G. Stearns, J. S. Taylor, and J. H. Underwood, "EUV scattering and flare of 10× projection cameras," in *Emerging Lithographic Technologies III*, Y. Vladimirski, ed., Proc. SPIE **3676,** 717–723 (1999).
9. These data are available at http://www-cxro.lbl.gov/optical_constants/.
10. P. Rai-Choudhury, *Handbook of Microlithography, Micromachining, and Microfabrication* (SPIE Press, Bellingham, Wash., 1997), pp. 74–82.
11. S. Jeong, L. Johnson, S. Rekawa, C. C. Walton, S. T. Prisbrey, E. Tejnil, J. H. Underwood, and J. Bokor, "Actinic detection of sub-100 nm defects on extreme ultraviolet lithography mask blanks," J. Vac. Sci. Technol. B **17,** 3009–3013 (1999).
12. S. H. Lee, J. Bokor, P. Naulleau, S. Jeong, and K. A. Goldberg, "Extreme ultraviolet holographic microscopy and its application to extreme ultraviolet mask-blank defect characterization," J. Vac. Sci. Technol. B **18,** 2935–2938 (2000).